Plasma Phys. Control. Fusion **49** (2007) 1245–1257 doi:10.1088/0741-3335/49/8/010

A 'multi-colour' SXR diagnostic for time and space-resolved measurements of electron temperature, MHD activity and particle transport in MCF plasmas

L F Delgado-Aparicio[1], D Stutman[1], K Tritz[1], M Finkenthal[1], R Bell[2], D Gates[2], R Kaita[2], B LeBlanc[2], R Maingi[3], H Yuh[4], F Levinton[4] and W Heidbrink[5]

[1] The Johns Hopkins University, Department of Physics and Astronomy, Baltimore, MD 21218, USA
[2] Princeton Plasma Physics Laboratory, Princeton, NJ 08543-0451, USA
[3] Oak Ridge National Laboratory/UT-Battelle, Oak Ridge, TN 37831, USA
[4] Nova Photonics, Inc., One Oak Place, Princeton, NJ 08540, USA
[5] University of California-Irvine, Department of Physics and Astronomy, Irvine, CA 92697, USA

E-mail: delgapa@pha.jhu.edu

Received 23 March 2007, in final form 31 May 2007
Published 3 July 2007
Online at stacks.iop.org/PPCF/49/1245

Abstract

A fast ($\leqslant$0.1 ms) and compact 'multi-colour' soft x-ray array has been developed for time and space-resolved electron temperature (T_e) measurements in magnetically confined fusion (MCF) plasmas. The electron temperature is obtained by modelling the slope of the continuum radiation from ratios of the available 1D-Abel inverted radial emissivity profiles over different energy ranges, with no *a priori* assumptions of plasma profiles, magnetic field reconstruction constraints or need of shot-to-shot reproducibility. This technique has been used to perform fast T_e measurements in the National Spherical Torus Experiment (NSTX), avoiding the limitations imposed by the well-known multi-point Thompson scattering, electron cyclotron emission and electron Bernstein wave mode conversion diagnostics. The applicability of this 'multi-colour' technique for magnetohydrodynamic (MHD) mode recognition and a variety of perturbative electron and impurity transport studies in MCF plasmas is also discussed. Reconstructed 'multi-colour' emissivity profiles for a variety of NSTX scenarios are presented here for the first time.

(Some figures in this article are in colour only in the electronic version)

1. Introduction

The present paper describes the newly developed compact 'multi-colour' optical (scintillator-based) soft x-ray (OSXR) array [1–3]. The motivation for the construction of this large bandpass 'multi-colour' soft x-ray (SXR) instrument is the development of simple,

 © 2007 IOP Publishing Ltd Printed in the UK

low cost and versatile diagnostics which can serve a wide range of magnetically confined fusion (MCF) experiments for a number of critical simultaneous profile measurements (e.g. T_e, n_e, n_Z). This diagnostic scheme was envisioned initially as a complementary diagnostic for an existing poloidal diode-based array on the National Spherical Torus Experiment (NSTX) spherical tokamak (ST), but with the specific aim of providing space and time-resolved measurements of the electron temperature profiles. The electron cyclotron emission (ECE) diagnostic cannot be used for fast electron temperature measurements in confinement schemes such as the compact ST, due to a combination of high plasma density and low magnetic field. With additional space and time resolved atomic data, analysis and spectroscopic input, the 'multi-colour' instrument described in this paper has the potential for providing 'ECE-like' functionality to any MCF plasma scheme, especially if the requirements imposed by the ECE-detection techniques are not fulfilled by the plasma density and local magnetic field. Since the fast electron temperature measurements can be constrained by the SXR emissivity ratios [3], a tangential view is desirable for inverting the line-integrated SXR brightness to obtain the radial x-ray emissivity profiles; this technique requires no *a priori* assumption of plasma density and temperature profiles, 2D magnetic flux surface reconstruction constraints or shot-to-shot reproducibility for a simultaneous SXR inversion over three energy ranges.

In NSTX, a multi-point Thomson scattering (MPTS) diagnostic system is used routinely for reliable electron temperature and density measurements. This diagnostic has low time resolution (16.7 ms), constrained by the 30 Hz repetition rate of two Nd : YAG lasers [4]. Therefore, it cannot be used during fast, time-dependent ($\leqslant$1 ms) heat deposition, magneto hydrodynamic (MHD) and perturbative transport studies. The electron Bernstein wave (EBW) mode conversion technique [5], also considered as a possibility for replacing the ECE method in STs, has likewise severe limitations. The location of the wave mode conversion 'layer', as well as the mode conversion efficiency, depend strongly on the local electron density gradient (∇n_e). Therefore any spatial or time variations of the latter due to MHD events, for example, will introduce spurious effects in the $T_e(R, t)$ profile. The 'multi-colour' SXR technique, on the other hand, uses the ratio of the power absorbed by two 'identical' detectors, thus eliminating in theory any dependence on the magnetic field intensity and the electron density or its gradient. In addition, the tangential 'multi-colour' SXR array is desirable for removing mid-plane SXR reconstruction inconveniences especially during NSTX high confinement (H-mode) operations [6]. A SXR tomographic inversion based on a limited number of existing poloidal chords is a difficult task. Even when it is possible to use the nested magnetic flux surface 2D reconstruction as a constraint for constant SXR emissivity contours, the approximation does not provide an appropriate fit due to hollow SXR profiles, and the top/bottom asymmetries in diverted discharges. Using accurate mid-plane SXR emissivity reconstructions, it is possible to obtain not only fast electron temperature measurements but also radial information on several plasma parameters used in MHD and perturbative transport studies [3].

This paper is organised as follows. In sections 2 and 3, we review the concept of the 'multi-foil' technique and the experimental setup used on the NSTX ST. A description of the analysis applied to the line-integrated data, as well as the numerically inverted emissivity reconstructions, is provided in section 4. Emphasis is placed on SXR emissivity reconstruction results during MHD-related neo-classical tearing modes (NTMs) and fishbone activity. Also, we include some preliminary results from perturbative particle transport experiments.

2. Principle of the 'ideal' multi-colour measurement

We assumed that the electrons are governed by a local Maxwellian electron energy distribution function (EEDF) and that the SXR spectrum is dominated by continuum radiation. In that case,

the Bremsstrahlung emitted by a local volume-element, filtered by a metallic foil and absorbed by the detector of choice is given by

$$\mathcal{E}_X(R,t) \propto \sqrt{T_e(R,t)}\gamma(T_e, Z)Z_{\text{eff}}(R,t)n_e^2(R,t)\exp\left\{\frac{-E_C}{k_B T_e(R,t)}\right\}, \tag{1}$$

where T_e, n_e and Z_{eff} are the local electron temperature, electron density and the average plasma ion charge, respectively. The factor $\gamma(T_e, Z)$ represents the enhancement of radiation over Bremsstrahlung due to free-bound recombination, assumed to be caused in NSTX predominantly by highly ionized carbon, since the machine is covered with carbon tiles. By using multiple foils with different cut-off energies (E_C) and several detectors with identical plasma views, it is possible to probe the same plasma volume at multiple energy ranges within the local energy dependence *slope* of the SXR continuum radiation. The ratio ($\Re_{(j/i)}$) of SXR powers absorbed by the detector with the thick (j) to thin (i) metallic foils is therefore given by

$$\Re_{(j/i)}(R,t) \equiv \frac{\mathcal{E}_{X,j}(R,t)}{\mathcal{E}_{X,i}(R,t)} \approx \exp\left\{\frac{-\Delta E_{C(j/i)}}{k_B T_e(R,t)}\right\}, \tag{2}$$

where $\Delta E_{C(j/i)} = E_{C,j} - E_{C,i} > 0$ is the cut-off energy difference between the thick and the thin foils. Any temporal or spatial variations of this ratio will only be due to a local electron temperature change. A discussion of the 'ideal' multi-colour technique regarding the selection of filters, line-emission contribution and the sensitivity to a temperature modulation of the ratios $\Re_{(j/i)}$ can be found in [6]. The presence of line emission could undermine this technique by overestimating the low-energy SXR emissivity. The appropriate selection of filters, as well as a low oxygen-to-carbon ratio of the order of a per cent or less, will enable the correct interpretation of the multi-colour ratios. In order to consistently check the very first assumption regarding the Maxwellain EEDF and thus the validity of the continuum radiation approximation, the amplitudes of the available signals can be routinely plotted against the foils cut-off energy as shown below [7–9].

The 'double foil' technique has been used successfully under a variety of plasma conditions and confinement schemes with a wide range of electron temperatures, from micro-pinches, macroscopic reversed field pinches (RFPs) and vacuum sparks, to modern tokamaks and stellarators. Despite all the efforts of numerous research groups, the vast majority of available references only deal with the central (core) electron temperature ($T_{e0} = T_e(r = 0)$), thus avoiding the complications involved in the measurement of the electron temperature space and time profiles $T_e(R,t)$ [7–9]. Recently, some progress has been made on providing time and space-resolved measurements of the electron temperature using the 'double-foil' technique [10,11]. These efforts nevertheless still depend on shot-to-shot reproducibility when attempting multi-colour SXR tomography, thus limiting the time resolution and/or significantly reducing the spatial coverage when the SXR cameras are grouped and filtered in pairs around the poloidal cross section. The tangential SXR array, however, lifts all these limitations by providing a simultaneous 'multi-colour' image of the plasma mid-plane profile, subject to a simple 1D-Abel reconstruction.

3. Experimental setup on the NSTX ST

In principle, such a diagnostic could be designed by using any kind of multi-channel SXR detector. The main advantage in using a scintillator, though, is the relatively inexpensive phosphor deposition on medium-to-large (∼5–15 cm) fiber optic windows on which a vacuum compatible, multi-chordal as well as a 'multi-colour' system [1–3] can be built. This SXR detection technique uses a fast (∼1–5 μs) and efficient scintillator (columnar—CsI : Tl, see [2])

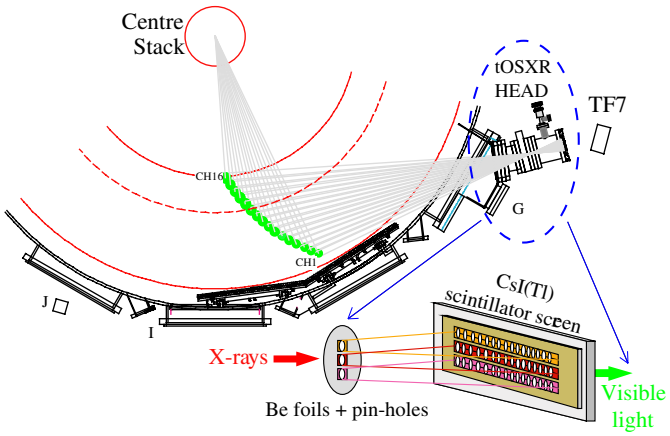

Figure 1. Tangential 'multi-colour' OSXR array installed in NSTX.

in order to convert soft x-ray photons to visible green light, with a peak emission wavelength at 550 nm. To obtain an appropriate sensitivity to electron temperature changes, the SXR emissivities should be measured at two or more energy ranges over which the difference of their cut-off energies is greater or at least equal to that of the plasma thermal energy. The 'multi-colour' capability is introduced by using a set of different beryllium foils with thicknesses of the order of 10, 100 and 300 μm. The SXR filters described above have low ($E_{C,10\%} \sim 780.64$ eV) medium ($E_{C,10\%} \sim 1690.0$ eV) and high ($E_{C,10\%} \sim 2416.1$ eV) cut-off energies (for 10% of SXR transmission) approximately equal to $1 \times \langle T_e \rangle_l$, $2 \times \langle T_e \rangle_l$ and $3 \times \langle T_e \rangle_l$, where $\langle T_e \rangle_l$ is the line-averaged electron temperature typical of NSTX discharges.

The tangential OSXR array installed in NSTX consists of 48 channels grouped in three rows of 16 channels each. Each mid-plane row, as depicted in figure 1, views the same plasma volume from the inboard side to the outboard edge. The chord spacing and pixel width, as depicted in figure 1, is ~4.5 cm. The three (1D) rows of 16 detectors are stacked one on top of the other, with a vertical 1 cm separation between them. This vertical displacement is conserved along the SXR detector sightline, from the three assigned pinholes and filters to the three rows of sixteen fibre optic centres per row. The forty-eight multi-clad fibre optic canes (FOCs) were also distributed in three rows, corresponding to the three pinhole-filter combination. The green photons ($\lambda_{CsI:Tl} \sim 550$ nm) from the SXR conversion are collected and transmitted by the use of the FOCs to the three sets of multi-anode photomultiplier tubes (PMTs). Attached to each of the PMTs are multi-channel transimpedance amplifiers, with a constant voltage to current gain of $\sim 10^7$ V A^{-1}. Additional detailed information regarding the geometry, SXR filtering, electro-optical characteristics and data acquisition elements can be found in [1–3].

4. Data analysis for NSTX plasmas

4.1. $T_e(R, t)$ estimates

A ~1.0 s flat-top, high power, high confinement (H) mode discharge (NSTX shot # 119991) has been considered for some of the results to be discussed. Figure 2(*a*) shows the time history for the plasma current (I_p) and the neutral beam injected power (P_{NBI}) for the entire discharge. A strong MHD instability is triggered at $t = 862$ ms, resulting in a neutron rate reduction

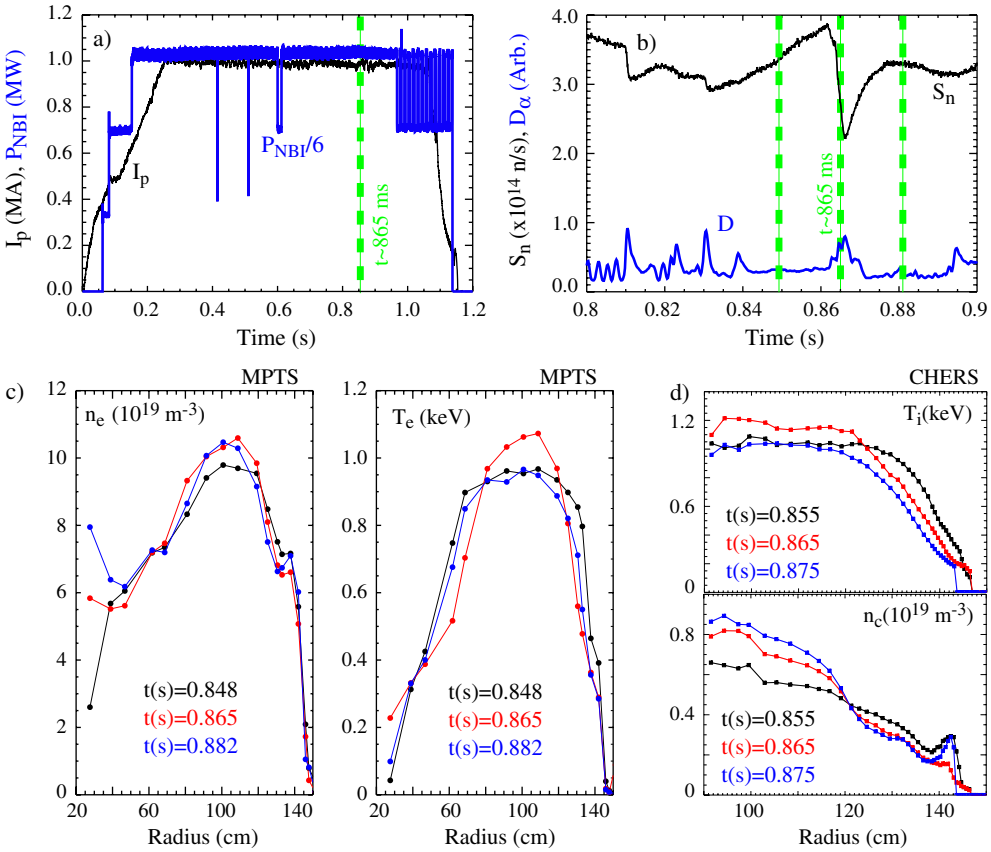

Figure 2. Time history for the (*a*) plasma current (I_p) and NBI power (P_{NBI}) and (*b*) neutron rate (S_n) and D_α signals. The (*c*) MPTS and (*d*) CHERS data are also shown.

of 42% of its original value (figure 2(*b*)). Such reduction in the neutron production rate and the rise of the D_α signal could be mostly due to the loss of fast ions from the plasma core. The times at which the MPTS and CHERS measurements were available are indicated by the dotted lines in figure 2(*b*) and the profiles in figures 2(*c*) and (*d*). Neither of the mentioned diagnostic systems can resolve such an event, due to the fast nature of the MHD phenomena, and its effect on the background plasma (∼1–5 ms). The SXR diagnostics have, on the other hand, fast time responses (on the order of 0.001–1 ms). This is enough to permit line-integrated measurements and 1D and 2D tomographic reconstructions of such MHD reconnection-like events.

4.1.1. Line integrated x-ray signals. Figures 3(*a*) and (*b*) present the line-integrated x-ray signals from a monitor (mid-plane) diode-based detector and the tangential OSXR array corresponding to a core tangency radius (R_{tg10}), filtered by the three available beryllium foils. The OSXR signals are corrected for the detectors sensitivity and gain. Even though these traces represent data from two different detectors and two distinct views (poloidal versus tangential), they show similar global time histories due to their same dependence on the electron temperature and density profiles. The (four) available Thomson scattering (MPTS) core electron temperature measurements, as well as the two signals corresponding to the

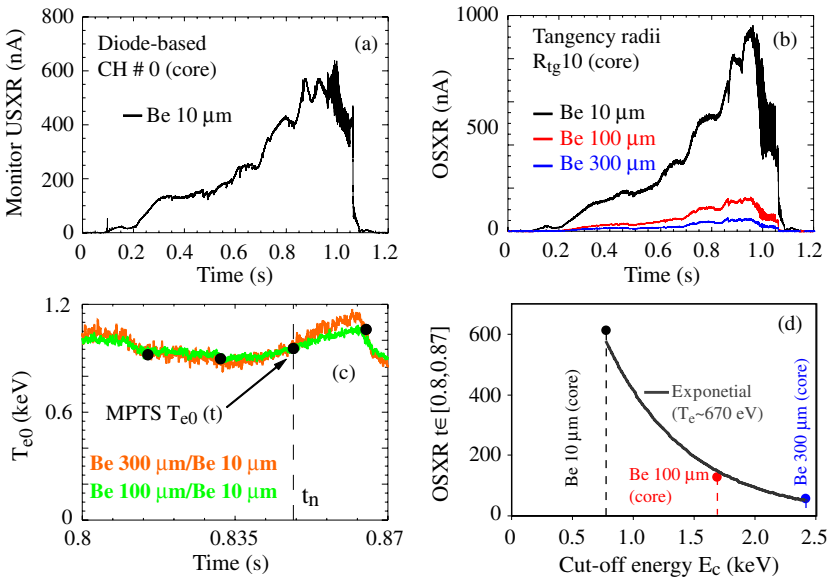

Figure 3. Time history of the line-integrated (*a*) monitor diode-based and (*b*) OSXR arrays. The so-called 100/10 and 300/10 multi-colour ratios normalized to the core MPTS values are shown in (*c*), and a consistent check of an exponential trend for the three available signals is depicted in (*d*).

$\Re_{100/10}$ (M/L) and the $\Re_{300/10}$ (H/L) SXR brightness ratios, normalized to MPTS are shown in figure 3(*c*). These two quantities are simply the ratios of the signals of figure 3(*b*) for the time interval $t \in [0.8,0.87]$ s. The dotted line in figure 3(*c*) indicates the time (t_n) at which the normalization was performed. The quasi-continuous time history from the multi-colour ratios normalized to an MPTS value shows the same trend as the available MPTS points, suggesting that the electron heating was indeed a steadily increasing process, instead of the *sudden* jump indicated by the Thomson scattering system (see figure 2(*c*)). The 10/100/300 exponential fit shown in figure 3(*d*) provides a consistent check and proof that the measurement is not contaminated by line emission and suprathermal electrons. The reasons for negligible line contamination is that carbon is by far the dominant impurity in NSTX (typically $N_C/N_O \geqslant 10-20$; see [6]), while all the cut-off energies are well above the most energetic carbon line emission. The line-integrated signals enable the measurement of fast electron temperature profiles in good agreement with the (slower) Thomson scattering measurements for a variety of plasma conditions. However, in the cases of strong inhomogeneities in the local plasma characteristics or broader SXR emissivity profiles, the limitations in the use of line-integrated signals become apparent.

4.1.2. SXR emissivity reconstructed profiles. A smoothing procedure using cubic spline functions has been applied to the line-integrated data, in which its degree of smoothing is such that the resultant function fits in within the data uncertainty. A first time history for the low-, medium- and high-energy reconstructed emissivity profiles shown in figure 4 was obtained using the smoothing spline technique and by means of a matrix-based inversion procedure [3]. The three dotted lines correspond to the MPTS times available within the time of interest $t \in [840, 890]$ ms, and the white arrow indicates the time at which the instability was triggered ($t_{ins} = 862$ ms), as indicated by the beginning of the neutron rate decay and the D_α raise. The

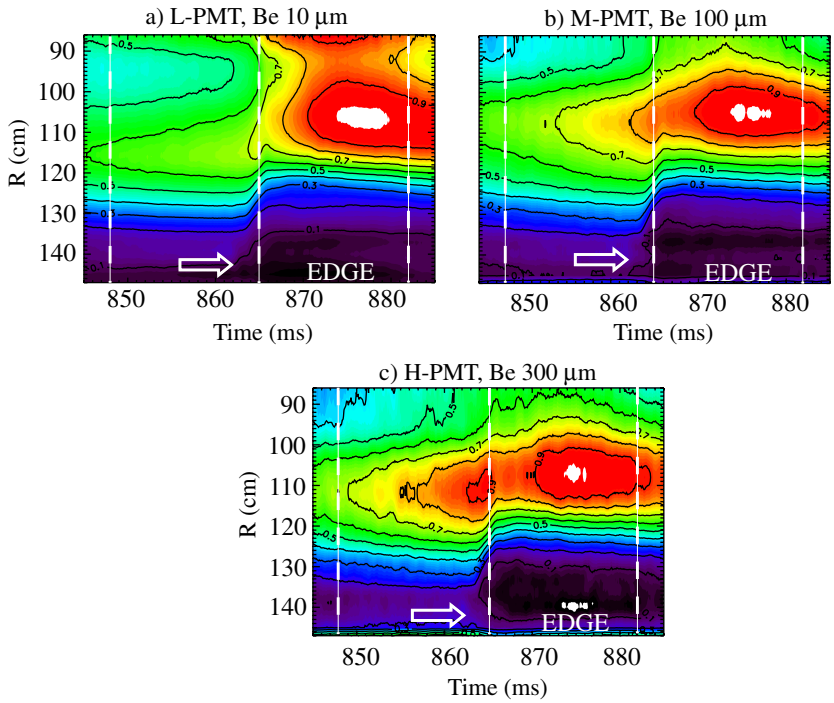

Figure 4. Time history of the normalized SXR emissivity reconstructions for the (*a*) L-PMT, (*b*) M-PMT and (*c*) H-PMT detectors for NSTX shot# 119991.

density increase at the core and away from the magnetic axis at the inboard side ($R \sim 90$ cm), consistent with both the MPTS and CHERS data, can also be seen in the low-energy emissivity shown in figure 4(*a*). On the other hand, the steady temperature increase and subsequent crash at mid-radius ($r/a \sim 0.5$, $R \sim 130$ cm) have been imaged using the medium- and high-energy detectors (due to their increased sensitivity to the local electron temperature response (see figures 4(*b*) and (*c*)). The time history for the medium- and high-energy profiles suggests that the core temperature increased steadily from the first to the second MPTS time points in agreement with the line-integrated results shown in figure 3(*d*). In addition, the 0.5 ms averaged perturbation imaged by the multi-colour arrays suggests that the mode travels from the mid-radius to the core in approximately 4 ms. After the mode has flattened the electron temperature, the medium and high-energy emissivities seemed to peak again at approximately 875 ms. This suggests a possible plasma reheating, but the SXR emissivity peaking is related to a rise in the electron density instead. A detailed q-profile time evolution has been determined from the newly developed motional Stark effect [12] diagnostic and the LRDFIT magnetic reconstruction routine [13]; these results suggest the presence of a NTM collapse between 860 and 870 ms (see figure 5(*a*)). The location of such reconnection-like events as deduced from the q-profile measurements is in agreement with the location of the temperature crash, established by the MPTS profiles and the SXR-reconstructed emissivities.

In order to find the proper constraint for the fast electron temperature time histories, we used the 'multi-colour' emissivity ratios. The time history of the 1D-Abel inverted ratios are shown in figure 5(*b*). Both ratios show the strong temperature perturbation at mid-radius ($R \sim 130$ cm, $r/a = 0.5$), consistent with both the q-profile collapse and the discrete MPTS

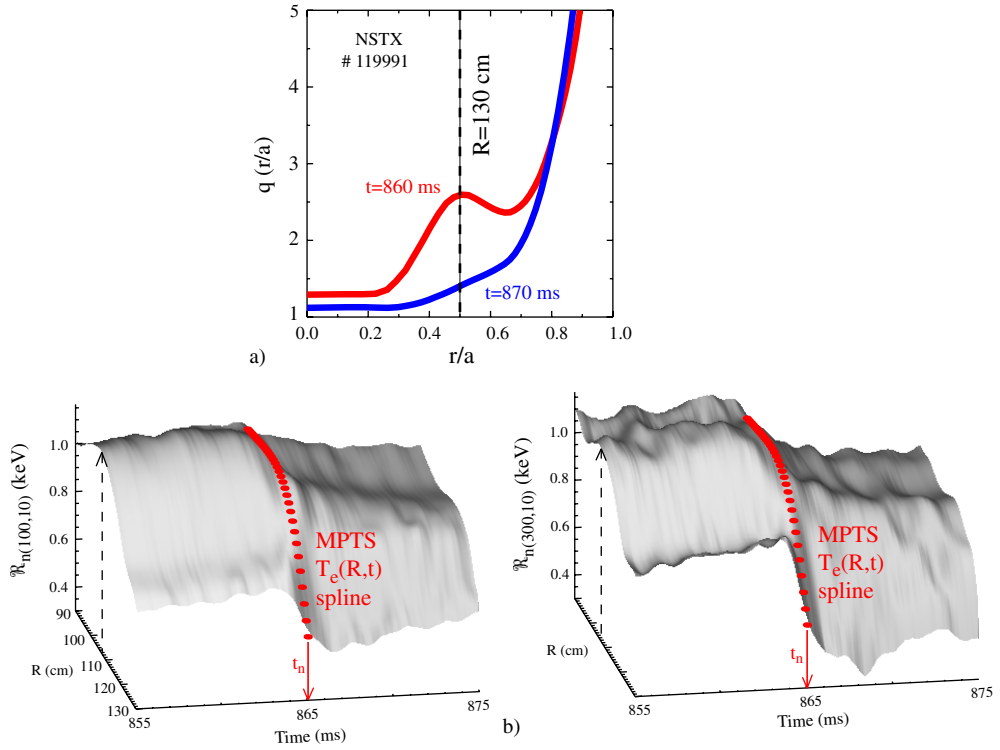

Figure 5. (*a*) MSE q-profile for the time of interest and (*b*) time history of the normalized (to the MPTS spline) Be100/Be10 (M/L) and (*b*) Be300/Be10 (H/L) ratios.

$T_e(R, t = t_n)$ spline values (red bullets); the MPTS and CHERS measurements were done at a time where the perturbation was still in its radial trajectory towards the magnetic axis, and is the reason why the core ion and electron temperatures seemed unaffected. After the core temperature flattens on a 1 ms timescale, it remains flat until the time of the other MPTS point at 882 ms. An interesting observation is that the perturbation from the high-to-low-energy ratio ($\Delta E_{C(H/L)} \sim 1635.5$ eV) seemed to be stronger than that of the medium to low-energy ratio ($\Delta E_{C(M/L)} \sim 909.36$ eV), but such an apparent discrepancy is only due to the improved ($\times 1.8$) contrast offered by the high-to-low energy ratio [3].

4.2. Particle transport experiments

Another example highlighting the versatile use of the 'multi-colour' SXR array involves controlled impurity injections during particle transport experiments. Similar, MHD quiescent NSTX H-mode plasmas had neon gas injected as an extrinsic impurity for observing its propagation from the outboard edge ($R \sim 160$ cm) to the core ($R \sim 100$ cm). The brightness profiles obtained from the tangentially line-integrated signals could provide only an order-of-magnitude estimate of the core particle diffusivity. Therefore, inverted SXR emissivities are imperative for determining the radial-dependent diffusivity, as well as the particle (convective) pinch velocity. The aim of this work is to study particle transport in a variety of scenarios, including changes in the toroidal magnetic field, plasma current, q-profile, collisionality and $\vec{E} \times \vec{B}$ shear. An example of the experimental results with inverted emissivities is depicted in

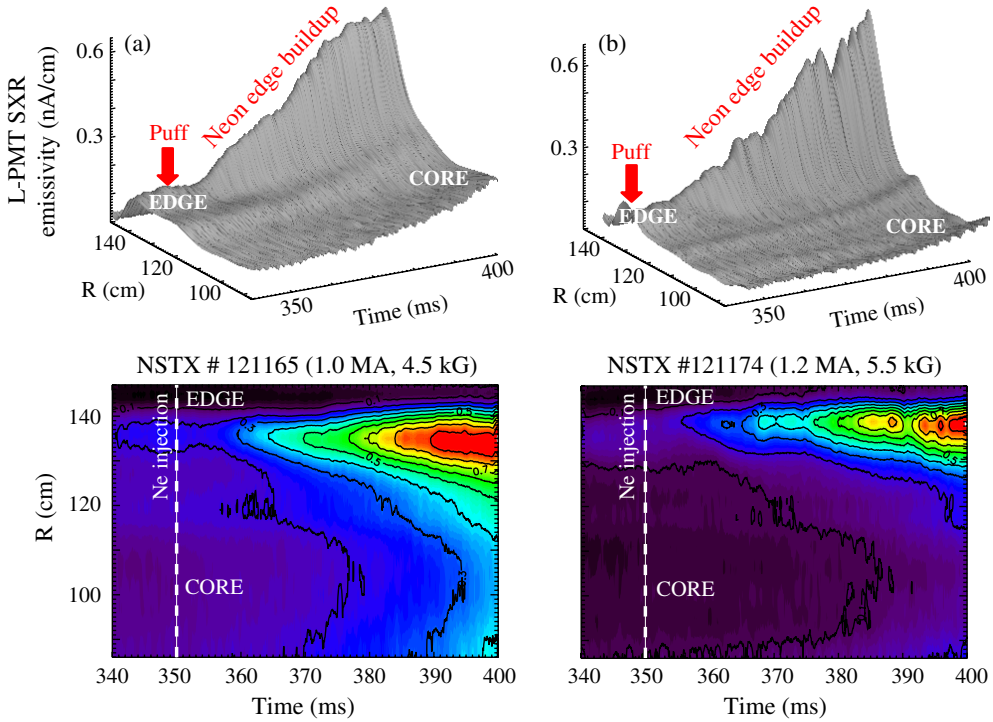

Figure 6. Surface and normalized contour plots of the reconstructed low-energy SXR emissivity for H-mode plasmas with Ne injection.

figure 6. The surface and normalized contour plots are shown for two different conditions of plasma current and toroidal field during fixed q-profile, ρ^* scaling experiments ((a) 1.0 MA, 4.5 kG versus (b) 1.2 MA, 5.5 kG).

The neon puffs (1.5 Torr l s^{-1}) began at 350 ms and lasted for 50 ms. The low-energy array (L-PMT) mostly observes the He− and H-like (Ne8+, Ne9+) neon accumulated at the outboard edge meanwhile, the fully stripped neon (Ne10+) contribution is imaged by the medium- and high-energy signals due to its higher cut-off energy (not shown here). A first qualitative estimate of the particle transport using the neon buildup at the NSTX edge (as seen in figure 6) indicates low impurity diffusivities on the range of 0.85–1.25 m^2 s^{-1}. The relationship between the latter values obtained from an ion gyro-radius scan at fixed q-profile is in very good agreement with the $\rho^2 q^2 \propto 1/B^2$ scaling of the neo-classical transport coefficients, for high (5.5 kG) and low (4.5 kG) toroidal magnetic fields, respectively. The contribution from the injected impurities to the SXR emission is obtained by subtracting the intrinsic background from reference reproducible discharges. An assessment of the core particle diffusivities with the TRANSP and the NCLASS codes as well as the convective pinch velocities with the impurity transport MIST code is underway [14].

The tangential 'multi-colour' OSXR array is also being used in assessing the conditions for impurity accumulation in the core with the subsequent flattening of the temperature profiles consistent with a resistive (1, 1) MHD mode. The plots depicted in figure 7 correspond to the MHD modes triggered by impurity accumulation ∼400 ms after the neon puffs in discharge # 121165. It is interesting to note that the low frequency oscillations observed by the low-energy detector sensitive to He− and H-like neon density fluctuations peak further inside

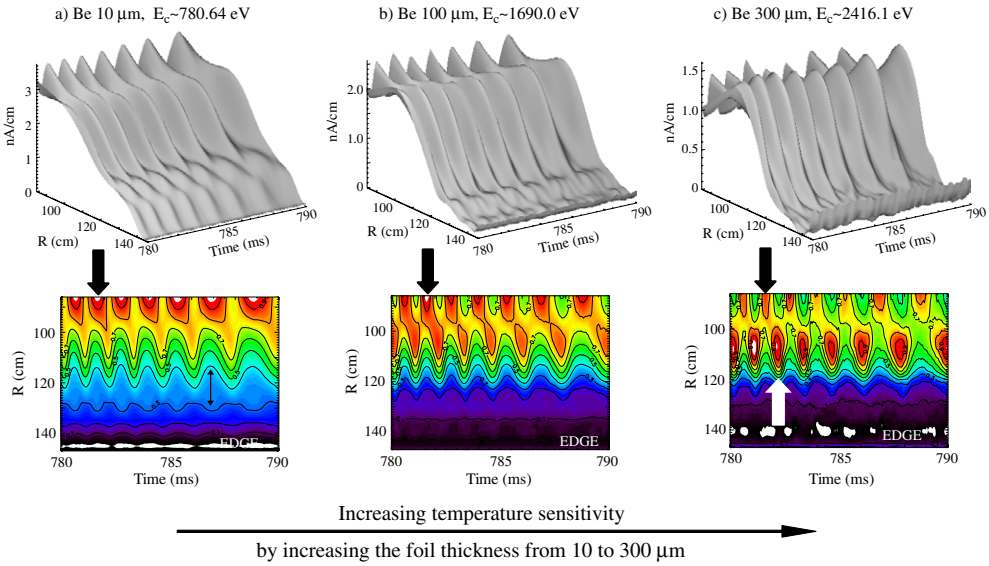

Figure 7. Surface and normalized contour plots of the reconstructed low-, medium- and high-energy SXR emissivity during the MHD activity triggered by impurity accumulation.

($R \leqslant 90$ cm) and not at the magnetic axis ($R \sim 105$ cm). On the other hand, the high-energy detectors sensitive to fully stripped neon density perturbations, as well as electron temperature variations, show a core temperature modulation with the same frequency as in the neon density perturbation, but with a 180° offset with respect to the latter (compare contours 7(*a*) and (*c*)). The difference in temperature sensitivities as well as the decoupled density and temperature features within an MHD event can be explained evaluating the variations of their measured radiated power,

$$\frac{\mathrm{d}\mathcal{E}_{X,j}(R,t)}{\mathcal{E}_{X,j}(R,t)} = \left(\frac{1}{2} + \frac{E_{\mathrm{C}_j}}{T_\mathrm{e}(R,t)}\right)\frac{\mathrm{d}T_\mathrm{e}(R,t)}{T_\mathrm{e}(R,t)} + 2\frac{\mathrm{d}n_\mathrm{e}(R,t)}{n_\mathrm{e}(R,t)}. \tag{3}$$

The coefficients affecting the $\mathrm{d}T_\mathrm{e}(R,t)/T_\mathrm{e}(R,t)$ term for both the medium- and high-energy emissivity fluctuations (using an average core plasma temperature of 800 eV) are approximately 2.61 and 3.5, respectively. In conclusion, for comparable density and temperature variations, the temperature fluctuations will be enhanced over the density fluctuations a factor of 30% when the medium-energy emissivity analysis is used, and a factor 75% in the case of the high-energy emissivity. This energy-dependent enhanced sensitivity observed in figures 7(*b*) and (*c*) is solely varied by increasing the foil thickness. The electron temperature measurements can therefore be made, both by computing the ratio of the signals from the high-to-medium-energy detectors and/or by subtracting the local variations of the energy-sensitive emissivities indicated in equation (3). The out-of-phase impurity density and electron temperature fluctuations can be explained by assuming a hot-island passing by the detector sightlines, which will locally reduce the density of highly radiating low-charge states, transiently ionizing them into fully stripped neon ions.

4.3. Fishbone activity

A low density ($n_{\mathrm{e}0} \sim 1.5 \times 10^{19}\,\mathrm{m}^{-3}$), high temperature ($T_{\mathrm{e}0} \sim 1.5$ keV), $I_\mathrm{p} \sim 0.8$ MA helium L-mode plasma (see figure 8(*a*)) was the target of choice to study the creation and time

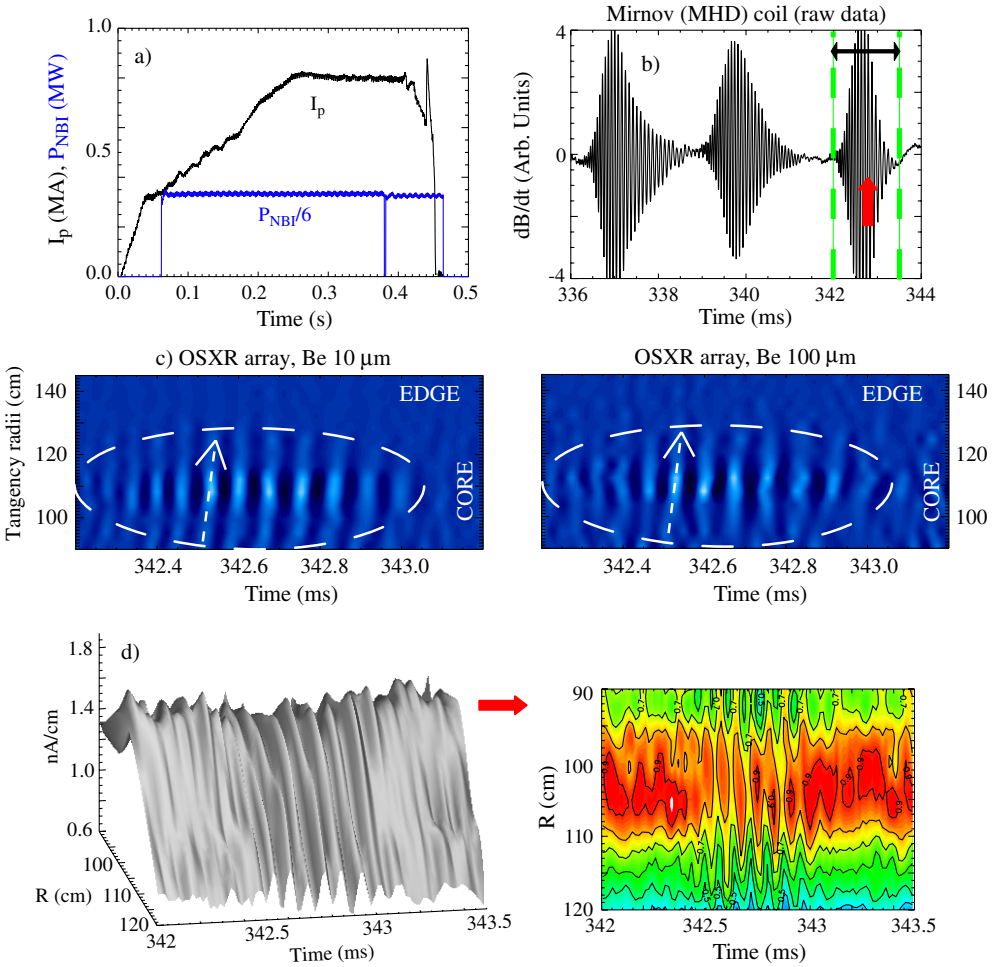

Figure 8. L-mode (*a*) plasma current and NBI power, (*b*) raw Mirnov coil and SXR (*c*) line integrated and (*d*) low-energy reconstructed profiles for the time of interest during a Fishbone burst.

evolution of the fast-ion induced fishbone instability (depicted in figure 8(*b*)). Fast-ion transport is important because it alters the power, momentum and particle sources of the background plasma [15,16], causing the redistribution of the electron temperature and impurities, similar in form to the sawtooth instability. Moreover, this instability is present in most of the advanced scenario plasma discharges involving reversed-shear q-profile studies. A typical ∼13 kHz rotating helical perturbation, shown in figure 8(*c*), is first imaged using the line-integration sightlines of the low- and medium-energy detectors. The toroidal trajectory of the instability is indicated by the white dotted lines, with the non-linear saturation reaching its maximum amplitude as the frequency slows down at the plasma core ($R_{tg} \sim 110$ cm).

Separate timescales could be considered for determining whether this instability has a macroscopic effect on the plasma background or corresponds rather to a fast and local electron density and/or temperature perturbation ($\tilde{n}_e$, $\tilde{T}_e$), following the fast magnetic perturbation. The shortest timescale is the period of each oscillation (∼ 75 μs) within the fishbone burst; meanwhile, the macroscopic background effect could be studied by comparing the main

quantities of interest both at the beginning and at the end of the wave packet ($\Delta\tau \sim 1$–5 ms). The latter is usually defined by the decrease in the neutron rate due to the reduction of the fast ion population [17, 18]. The intensity modulation of the line-integrated signals within the fishbone burst appear to have a non-varying 'multi-colour' ratio, suggesting a fast electron density perturbation at nearly constant electron temperature. The surface and normalized contour plots of the reconstructed low-energy (L-PMT) emissivity are also shown in figures 8(*d*). It can be observed that the maximum perturbation ($\tilde{n}_e$ and/or $\tilde{T}_e$) indeed occurs at the time of the non-linear mode saturation, which coincides with the minimum mode chirped frequency (∼13 kHz) at the plasma core ($R \sim 105$ cm). Each fishbone burst seemed on the other hand to affect the background temperature distribution only in time intervals of the order of 1–5 ms, which are generally correlated with the decrease in the fast ion population and neutron rates [15, 16]. An instrument with a higher signal-to-noise ratio would be able to probe fast temperature perturbations within the fishbones oscillations as well.

5. Conclusions

The parameters describing the relationship between the SXR emissivity ratios and the changes in the local electron temperature, for the so-called 'ideal double-foil method', rely strongly on the assumption of the heavyside-like transmission function for each of the metallic filters. A simple model based on the SXR photo-absorption cross section and an exponential dependence of the SXR transmission as a function of photon energy is currently being developed for an accurate and analytical description of the SXR emissivity ratios [19]. In the present work the 1D-Abel reconstructions of fast MHD phenomena have been considered only as a first order approximation of the real 2D and 3D reconstructions; thus the inversion presented here represents only an averaged (smoothed) picture. The assumption of toroidal axisymmetry is consistently broken when the local emissivity is perturbed by a 'corkscrew-like' helical mode around the torus-shaped plasma. For instance, if the steady-state SXR emissivity $\mathcal{E}_0(r)$ is constant on a surface with a Gaussian distribution on minor radius, $\mathcal{E}_0(r) \sim \exp\{-(r/l_\mathcal{E})^2\}$, the helical perturbation superimposed on a resonant surface could be such that its associated emissivity can be described by $\mathcal{E}_1(r, \theta, \phi) \sim \exp\{-(r - r_s)^2/l_w^2\}\cos(m\theta - n\phi)$, with (m, n) being the poloidal and toroidal Fourier components. Future studies will include also the SXR forward modelling in which the MHD mode recognition will be made on the basis of a fit of the tangentially integrated data to a specific (m, n) perturbation [20, 21].

In summary, a first prototype tangential 'multi-colour' SXR system has been successfully tested in the NSTX ST at PPPL. The tangential view is desirable in MCF plasmas since a 1D Abel reconstruction can account for the SXR emissivity profiles. The results shown were obtained in L-mode and H-mode plasmas suggesting that the 'multi-colour' technique could be used in different scenarios for simultaneous MHD mode recognition, particle transport and heat deposition studies. This instrument is currently being used for a variety of particle and heat perturbative transport experiments as well as on establishing the impact of MHD instabilities such as edge localized modes (ELMs) and NTMs in the background plasma. An order of magnitude higher SNR is achievable by considering more efficient electro-optical components, therefore enabling the possibility of faster ($\leqslant$20–50 μs) $T_e(R, t)$ measurements.

Acknowledgments

The authors would like to thank the technical teams at both The Johns Hopkins University and the Princeton University Plasma Physics Laboratory (PPPL) for their valuable help in

implementing this programme. One of the authors (LFDA) would also like to thank Dr J Menard for the development of the LRDFIT magnetic reconstruction routine used in this paper. This work was supported by the United States Department of Energy (DOE) Grants No DE-FG02-86ER52314ATDOE and DE-AC02-76-CH0-3073.

References

[1] Delgado-Aparicio L F *et al* 2004 *Rev. Sci. Instrum.* **75** 4020
[2] Delgado-Aparicio L F *et al* 2007 *Appl. Opt.* at press
[3] Delgado-Aparicio L F *et al* 2007 *J. Appl. Phys.* submitted
[4] LeBlanc B *et al* 2003 *Rev. Sci. Instrum.* **74** 1659
[5] Taylor G *et al* 2001 *Rev. Sci. Instrum.* **72** 285
[6] Stutman D *et al* 2003 *Rev. Sci. Instrum.* **74** 1982
[7] Kiraly J *et al* 1987 *Nucl. Fusion* **27** 397
[8] Martin P *et al* 1996 *Plasma Phys. Control. Fusion* **38** 1023
[9] Murari A *et al* 1999 *Rev. Sci. Instrum.* **70** 581
[10] Bonomo F *et al* 2006 *Rev. Sci. Instrum.* **77** 10F313
[11] Franz P *et al* 2006 *Rev. Sci. Instrum.* **77** 10F318
[12] Levinton F 2007 *Phys. Plasmas* **14** 056119
[13] Menard J 2007 *private communication*
[14] Delgado-Aparicio L F *et al* 2007 to be submitted
[15] Günter S *et al* 1999 *Nucl. Fusion* **39** 1535
[16] Günter S *et al* 1999 *Plasma Phys. Control. Fusion* **41** B231
[17] Heidbrink W W 1994 *Nucl. Fusion* **34** 535
[18] Kass T *et al* 1998 *Nucl. Fusion* **38** 807
[19] Delgado-Aparicio L F *et al* 2007 *Rev. Sci. Instrum.* to be submitted
[20] Igochine V *et al* 2003 *Nucl. Fusion* **43** 1801
[21] Weller A *et al* 1999 *Rev. Sci. Instrum.* **70** 484